Phys Chem Minerals (2003) 30: 486–494
DOI 10.1007/s00269-003-0342-2

ORIGINAL PAPER

S. Demouchy · S. Mackwell

Water diffusion in synthetic iron-free forsterite

Received: 16 September 2002 / Accepted: 10 June 2003

Abstract The kinetics of hydrogenation of dry synthetic forsterite single crystals was determined by performing experiments under hydrothermal conditions. The experiments were performed at 1.5 GPa, 1000 °C for 3 h in a piston-cylinder apparatus, or at 0.2 GPa, 900–1110 °C, for 3–20 h in TZM cold-seal vessels. The oxygen fugacity was buffered using Fe–FeO or Ni–NiO powders. Polarized Fourier transform infrared spectroscopy was utilized to quantify the hydroxyl distributions in the samples after the experiments. Hydrogenation rates were measured parallel to the three crystallographic axes from profiles of water content as a function of position in the samples. The chemical diffusion coefficients are marginally slower than in natural iron-bearing olivine for the same diffusion process, but the anisotropy of diffusion is the same, with the [001] axis the fastest direction of diffusion and [100] the slowest. Fits of the diffusion data to an Arrhenius law yield similar activation energies for each of the crystallographic axes; a global fit to all the diffusion data gave 211 ± 18 kJ mol^{-1}, in reasonable agreement with the previous results for natural olivine. Thus hydrogenation most likely occurs by coupled diffusion of protons and octahedrally coordinated metal vacancies. The diffusion rates are fast enough to modify water contents within xenoliths ascending from the mantle, but probably too slow to permit a total equilibration of forsterite or olivine crystals.

Keywords Point defects · Diffusion · Water · Forsterite · Polarized Infrared spectroscopy

S. Demouchy (✉) · S. Mackwell
Bayerisches Geoinstitut, Universität Bayreuth,
D-95440 Bayreuth, Germany
e-mail: Sylvie.Demouchy@uni-bayreuth.de
Tel: +49 (0)921-55-3878
Fax: +49 (0)-921-55-3769

Present address: S. Mackwell
Lunar and Planetary Institute,
3600 Bay Area Blvd, Houston, Texas 77058, USA

Introduction

Knowledge of the water or hydroxyl (OH) contents of nominally anhydrous minerals (NAMs), olivine, garnet and pyroxene, is important in order to understand the physical and chemical behaviour of the Earth's interior (Miller et al. 1987; Bell and Rossman 1992; Kohlstedt et al. 1996; Ingrin and Skogby 2000). Many studies have investigated interactions between water and mantle minerals, especially with respect to subduction zone processes, mantle rheology, phase equilibria and petrologic processes (e.g. Chopra and Paterson 1984; Mackwell et al. 1985; Karato et al. 1986; Arndt et al. 1998; Gaetani and Grove 1998; Muentener et al. 2001). However, few studies have considered that the concentration and speciation of water-derived species in minerals may adjust in response to changes in the hydrothermal environment.

Experimental studies of olivine, the major upper-mantle mineral, indicate that significant amounts of hydroxyl can dissolve within olivine as point defects (Bell and Rossman 1992; Kohlstedt et al. 1996). Such point defects diffuse in response to changes in the hydrothermal environment (Philibert 1991). Mackwell and Kohlstedt (1990) and Kohlstedt and Mackwell (1998, 1999) demonstrated that, in experiments at low temperatures for short experimental durations, hydrogen incorporation occurs by redox exchange of protons with polarons (electron holes localized on iron atoms occupying octahedrally coordinated cation (metal) sites). As the maximum polaron content of olivine (nominally the ferric iron concentration) is on the order of 100 atomic ppm at low pressure (Nakamura and Schmalzried 1983; Tsai and Dieckmann 1997, 2002), this process permits the incorporation of only limited concentrations of water-derived species. This process is also rate-limited by proton diffusion and yields proton self-diffusivities of around 10^{-10}m^2 s^{-1} at 1000 °C; proton diffusion is also strongly anisotropic with fastest direction of diffusion parallel to [100] (Mackwell and Kohlstedt 1990).

At higher temperatures and/or longer experimental durations, additional hydrogen is incorporated by a second process that involves defect associates of protons and intrinsic defects, assumed to be metal vacancies by Kohlstedt and Mackwell (1998). In this case, the sample can incorporate more water, with up to 135 wt ppm H_2O (2200 H/10^6Si) at 2.5 GPa and 1100 °C (Kohlstedt et al. 1996). The incorporation of hydrogen by this coupled proton-vacancy process occurs at around 10^{-12}m^2 s^{-1} in olivine at 1000 °C, with the fastest direction of diffusion parallel to [001]. As there are essentially no polarons in iron-free olivine, only this second process is expected to occur in forsterite. Other experimental studies have shown that water solubility in the olivine-water system increases with increasing confining pressure, temperature, oxygen and hydrogen fugacity (Bai and Kohlstedt 1992; Locke et al. 2002), and with increasing iron content (Zhao et al. 2001). The present study aims to constrain more fully the speciation and transport rate of the mobile water-derived defects in synthetic forsterite, where there is no iron and, hence, no polarons.

Experimentals

Starting material and experiments

We use dry synthetic forsterite samples that have no cracks or optically visible inclusions. The chemical composition of this starting material, essentially pure Mg_2SiO_4, was checked with a Cameca SX50 electron microprobe (15 eV, 15 nA point beam and 20 s counting time, average over 20 points). ICP-AES analysis revealed a high boron content (737 at ppm in Fo2 samples), which is not too surprising as boron was most likely used as a flux during crystal growth.

The samples were cut with faces perpendicular to each crystallographic axis (±5°) and carefully polished using diamond films from 30 to 0.5 μm. The final sample size was around $2.5 \times 3 \times 2$ mm^3 parallel to [100], [010] and [001], respectively. The forsterite samples were equilibrated by cooking at 1300 °C for 20 h at room pressure with the oxygen fugacity around $10^{-7.3}$ atm controlled by a CO–CO_2 gas mixture. This step is necessary in order to equilibrate point defects in the crystal structure to values near those during the subsequent hydrothermal anneals. Infrared analysis was performed to verify the dry state of the samples.

The hydrogenation experiments (Table 1) were performed in a piston-cylinder apparatus or in tungsten-zirconium-molybdenum (TZM) cold-seal vessels. We performed experiments in the piston-cylinder apparatus at a pressure of 1.5 GPa and a temperature of 1000 °C for 3 h. Talc-Pyrex cells were used with an alumina cylinder and plugs around the capsule and a tapered graphite furnace. In order to avoid cracks during the quench, we decreased the temperature over about 5 min and decreased the pressure over 5 days. Unfortunately, even with such caution, it is still difficult to preserve single crystals without cracking. We welded the samples inside an iron capsule (only for sample Fo1-3) or $Pt_{0.95}$–$Rh_{0.05}$ capsules along with 10 μl of water.

For hydration in TZM cold-seal vessels, we worked at a pressure of 0.2 GPa, and temperatures between 900 and 1100 °C for experimental durations between 1 and 20 h. The capsules in these experiments were pure platinum and we included 20 μl of water.

Samples were packed in synthetic iron-free enstatite powder to buffer the activity of silica and NiO–Ni (powder/foil) or mixed Ni–NiO powder (for Fo1–3, Fe–FeO powder) to control the oxygen fugacity during the experiments (Table 1). The oxygen fugacities, fO_2, for each experiment were calculated using the data from O'Neill (1987) for the Ni–NiO buffer and from O'Neill and Wall (1987) for the Fe–FeO buffer. After each experiment, we checked for the presence of both Ni and NiO (or Fe and FeO) in the capsule using optical microscopy to verify that neither component of the buffer had been totally consumed.

Transmission electron microscope (TEM) observations were performed on forsterite sample Fo2-10 after the experiment to check whether our samples contained boron-rich precipitates, hydrous defect layers (e.g. humite lamellae; Miller et al. 1987), high dislocation densities or melt pockets (e.g. the early partial melting phenomenon of Raterron et al. 2000). The observations were carried out in the hydrated regions near the sample edges as well as in the anhydrous interior. The TEM observations demonstrated that Fo2-10 is free of precipitates, linear and planar defects.

Infrared spectroscopy

The hydroxyl distributions within our samples were analyzed using polarized Fourier transform infrared (FTIR) spectroscopy performed using a Bruker IFS 120 HR high-resolution FTIR spectrometer coupled with a Bruker IR microscope. The FTIR contains all-reflecting Cassegranian optics and is equipped with a metal-strip polarizer on a KRS-5 substrate. Analyses in the microscope were made at room temperature and pressure, under a stream of H_2O- and CO_2-free purified air. Near-infrared (NIR) measurements were performed using a tungsten light source, an Si/CaF_2 beamsplitter and high-sensitivity narrow-band MCT (mercury-cadmium-telluride) detector cooled by liquid nitrogen. Two hundred scans were accumulated for each spectrum at a resolution of 1 cm^{-1}.

Table 1 Experimental conditions of hydrogenation for forsterite samples

Sample	Apparatus	Temperature (°C)	Pressure (GPa)	Time (h)	Buffer	Log fO_2^c	Capsule
Fo1-3	PC[a]	1000	1.5	3	Fe–FeO	−14.2	Fe
Fo2-2	PC	1000	1.5	3	Ni–NiO	−10.3	$Pt_{0.95}$–$Rh_{0.05}$
Fo2-4	TZM[b]	1000	0.2	8	Ni–NiO	−10.3	Pt
Fo2-5	TZM	1060	0.2	8	Ni–NiO	−9.4	Pt
Fo2-6	TZM	1060	0.2	8	Ni–NiO	−9.4	Pt
Fo2-8	TZM	1100	0.2	3	Ni–NiO	−8.9	Pt
Fo2-9	TZM	1110	0.2	3	Ni–NiO	−8.7	Pt
Fo2-10	TZM	1110	0.2	3	Ni–NiO	−8.7	Pt
Fo2-12	TZM	900	0.2	20	Ni–NiO	−11.9	Pt
Fo2-13	TZM	950	0.2	12	Ni–NiO	−11.0	Pt
Fo2-14	TZM	900	0.2	20	Ni–NiO	−11.9	Pt

[a]PC = Piston cylinder
[b]TZM = tungsten-zirconium-molybdenum cold-seal vessel
[c]log fO_2 calculated using O'Neill (1987) for Ni–NiO, O'Neill and Wall (1987) for Fe–FeO

The infrared beam was focused in the middle of the sample using a 1.5-mm aperture, which generates to a spot size of 100 μm in the focal plane. Due to the divergence of the infrared beam, the associated spot size on the surface of a 1-mm sample is around 600 μm. In order to increase spatial resolution parallel to the diffusion direction, we used an aluminium mask fixed to the objective lens of the microscope to reduce the angle of incidence from 30° to 10°, yielding a spot size at the sample surface of around 270 μm parallel to the direction of diffusion.

First, we characterize each sample by taking a spectrum with the electric vector (E) parallel to each axis and then make hydroxyl profiles with E parallel to [001] and diffusion parallel to the [100], [010] and [001] crystallographic axes. Spectra were collected at a spacing of 30–50 μm near the edges and 100–300 μm near the centre of the sample. After a background baseline correction and thickness normalization to 1 cm, the hydroxyl content C_{OH} was determined for each spectrum using the relationship (see e.g. Brunner et al. 1961; Paterson 1982)

$$C_{OH} = \frac{1}{I} k(\nu)\, d\nu \quad (1)$$

$$\text{with } I = I_{//} a, \quad (2)$$

where $k(\nu)$ is the absorption coefficient at wavenumber ν, $I_{//}$ is the integral extinction coefficient (here assumed to be 5.32 cm^{-2} wt ppm^{-1} H_2O, Bell et al. 2003), γ is the orientation factor (equal to 1 in the case of polarized spectra with the polarization direction parallel to the O–H bond direction, see, e.g. Paterson 1982; Bell et al. 1995). Integration was performed between 3650 and 3050 cm^{-1}. The solubility of hydroxyl in forsterite is the sum of the concentrations determined using Eq. (1) for infrared measurements with the beam parallel to the three orthogonal crystal axes.

Diffusion analysis

The diffusivity of hydrogen (water-derived species) in forsterite can be determined from the plots of water content versus distance across the samples, as in previous works on iron-bearing olivine (Mackwell and Kohlstedt 1990; Kohlstedt and Mackwell 1998, 1999). The plots are fitted using a solution to Fick's second law for diffusion from an infinite source into a finite slab (Carslaw and Jaeger 1959); for a profile in one dimension:

$$C_{OH}(x) = C_0 \left[\operatorname{erfc} \frac{x}{2\sqrt{\tilde{D}_i t}} + \operatorname{erfc} \frac{X - x}{2\sqrt{\tilde{D}_i t}} \right] \quad (3)$$

where C_{OH} (x) is the hydroxyl concentration at a distance x from the first sample edge, X is the width of the sample, t is time, erfc is the complementary error function, C_0 is the maximum water content for the given infrared beam polarization and $\tilde{D}_i$ is the chemical diffusivity for the mobile species parallel to i = [100], [010] or [001] under the experimental conditions. This relationship is valid if the profiles from each side do not overlap significantly. According to Kohlstedt and Mackwell (1998), the chemical diffusivity, $\tilde{D}$, for the incorporation of hydrogen linked to metal vacancies is given by

$$\tilde{D} = \frac{3 D_{V_{Me}} D_H}{2 D_{V_{Me}} + D_H}, \quad (4)$$

where $\tilde{D}$ is the chemical diffusivity measured in the experiments, $D_{V_{Me}}$ is the diffusivity of metal vacancies and D_H is the self-diffusivity of protons. On the assumption that $D_H \gg D_{V_{Me}}$ (Nakamura and Schmalzried 1983; Kohlstedt and Mackwell 1998, 1999),

$$\tilde{D} \approx 3 D_{V_{Me}}. \quad (5)$$

Results

Infrared spectra and water solubility

Figure 1 shows typical polarized FTIR spectra for our hydrogenated forsterite samples from crystal Fo1 and Fo2. The major O–H absorption bands for samples from Fo2 are at 3613 and 3579 cm^{-1} for **E** parallel to [100] and at 3155 and 3567 cm^{-1} for **E** parallel to [001]. Sample Fo1-3, which had been treated at more reducing conditions, shows only a very weak band at 3613 cm^{-1} with **E** parallel to [100] and a strong band at 3215 cm^{-1} with **E** parallel to [001]. Positions for all O–H bands observed in our hydrogenated forsterite samples are shown in Table 2. The band positions do not change with experimental duration or temperature in this study. The water solubilities, calculated from the infrared spectra with beam polarization parallel to all three crystal axes using the calibration of Bell et al. (2003), vary from 1.3 ± 0.2 wt ppm water (20 ± 3 $H/10^6Si$) in sample Fo2-12 to 6.4 ± 0.9 wt ppm water (100 ± 14 $H/10^6Si$) in sample Fo1-3 (Table 3). In general, water solubility increases with increasing temperature at fixed pressure, except for sample Fo2-8, which has an inexplicably lower water content than other samples treated under essentially the same conditions. The water solubility reported for Fo2-2 is a minimum value, as poor sample quality made it impossible to measure hydroxyl concentrations with **E** polarized parallel to all three crystal axes. Similarly, as Fo2-2 is the only sample treated at 1.5 GPa with a Ni/NiO buffer, it is not possible to determine a pressure dependence of solubility from this study.

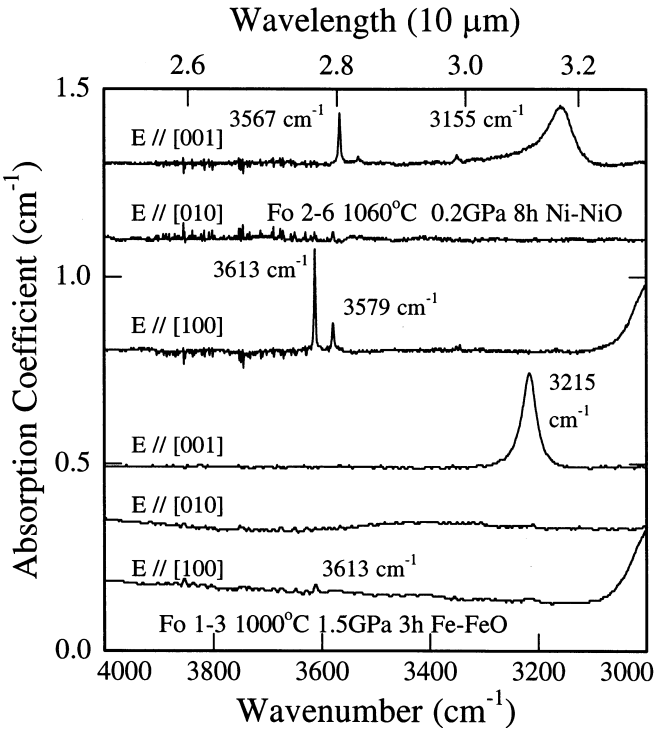

Fig. 1 Polarized IR spectra, with different orientations of electrical vector **E**, for forsterite samples Fo1-3 (after an experiment at 1000 °C, 1.5 GPa, 3 h duration, buffered by Fe–FeO) and Fo2-6 (after an experiment at 1060 °C, 0.2 GPa, 8 h duration and buffered by Ni–NiO). The noise of the spectra for Fo2-6 results from the poor quality of the sample. All the spectra are normalized to a thickness of 1 cm

Table 2 Hydroxyl band positions for different orientations of the infrared electric vector (**E**) in synthetic forsterite from this study and iron-bearing olivine from previous investigations. Wavenumber resolution ± 2 cm^{-1}

Fo1-3[a]			Fo2[a]		San Carlos olivine[b]	Pamir olivine[c]
E // [100]	[001]	[100]	[010]	[001]	Unpolarized	All polarization directions
						3674
						3647
					3637	3640
					3623	3624
3613		3613			3612	
					3598	3598
						3592
		3579	3577		3576	
						3570
				3567	3565	
			3552		3542	
				3534		3535
				3531	3529	
						3524
						3514
					3483	3478[d]
					3459	
					3443	
					3424	
						3404[d]
					3389	
				3350	3354	
		3344				3341[d]
					3329	
					3236	
	3215					3215[d]
				3155		

[a]Synthetic forsterite samples from this study
[b]Xenoliths from San Carlos, Arizona (Bai and Kohlstedt 1993)
[c]From skarn deposit in Pamir, Tadzikistan (Libowitzky and Beran 1995)
[d]Indicates a weak infrared band

Table 3 Water solubility in forsterite and chemical diffusivities along each axis

Sample	Water solubility[b] wt ppm H_2O($H/10^6Si$)	$\tilde{D}$[100] m^2 s^{-1}	$\tilde{D}$[010] m^2 s^{-1}	$\tilde{D}$[001] m^2 s^{-1}
Fo 1-3	6.4 ± 0.9 (100 ± 14)	$(4 \pm 1) \times 10^{-13}$	$(3.0 \pm 0.2) \times 10^{-13}$	$(5.0 \pm 0.2) \times 10^{-13}$
Fo 2-2[a]	>1.1 ± 0.2 (> 17 ± 3)	$(7.0 \pm 0.2) \times 10^{-13}$	$(3.0 \pm 0.2) \times 10^{-13}$	np
Fo 2-4	2.8 ± 0.4 (44 ± 6)	$(1.0 \pm 0.4) \times 10^{-13}$	$(1 \pm 1) \times 10^{-13}$	$(1.0 \pm 0.2) \times 10^{-12}$
Fo 2-5	5.7 ± 0.8 (89 ± 12)	$(2.0 \pm 0.5) \times 10^{-13}$	$(1.0 \pm 0.5) \times 10^{-12}$	$(3.0 \pm 0.8) \times 10^{-12}$
Fo 2-6	5.5 ± 0.8 (86 ± 12)	$(2.0 \pm 0.5) \times 10^{-13}$	$(6 \pm 1) \times 10^{-13}$	$(2.0 \pm 0.5) \times 10^{-12}$
Fo 2-8	2.3 ± 0.3 (36 ± 5)	$(5 \pm 2) \times 10^{-13}$	$(1.0 \pm 0.2) \times 10^{-12}$	$(1.3 \pm 0.2) \times 10^{-11}$
Fo 2-9	5.7 ± 0.8 (89 ± 12)	$(8 \pm 4) \times 10^{-14}$	$(1.6 \pm 0.5) \times 10^{-12}$	$(3.5 \pm 0.5) \times 10^{-12}$
Fo 2-10	3.6 ± 0.5 (56 ± 8)	$(1 \pm 1) \times 10^{-13}$	$(3.6 \pm 2.0) \times 10^{-13}$	$(1.0 \pm 0.5) \times 10^{-12}$
Fo 2-12	1.3 ± 0.2 (20 ± 3)	nwd[c]	nwd	$(2.0 \pm 0.6) \times 10^{-13}$
Fo 2-13	4.2 ± 0.6 (66 ± 9)	np[d]	$(2 \pm 1) \times 10^{-13}$	$(7 \pm 1) \times 10^{-13}$
Fo 2-14	3.8 ± 0.5 (59 ± 8)	$(2 \pm 1) \times 10^{-13}$	$(2 \pm 1) \times 10^{-13}$	$(2.5 \pm 0.5) \times 10^{-13}$

[a]Because of the poor quality of the sample, it was not possible to do infrared analysis with **E** // [001] so measurements were made only with **E** // [100]. Thus the quoted water solubility is an underestimation of the true water content
[b]Water solubility using Eq. (1) and the calibration of Bell et al. (2003)
[c]nwd*:* no water detected by infrared spectroscopy as there was insufficient hydroxyl for measurement along this axis
[d]np*:* because of the poor quality of the sample, it was not possible to fit a profile

Diffusion rates and anisotropy

Figure 2 presents a series of polarized infrared spectra for sample Fo2-9 with E // [001] and diffusion parallel to [001]. The figure shows absorption coefficient as a function of wavenumber and position in the sample. Intensity and area of hydroxyl infrared bands are highest at the edges and decrease toward the middle of the sample. Chemical diffusivities for each sample and each diffusion direction are given in Table 3. The diffusion is anisotropic, with fastest diffusion parallel to [001] and slowest diffusion generally parallel to [100]. An example of hydroxyl diffusion profiles for each axis is plotted in Fig. 3 for sample Fo2-10, with **E** parallel to [001]. The black lines represent the best fits of the diffusion law to the data using Eq. (3), which yielded the chemical diffusivities given on the figure. The fits were performed on the assumption of the same hydroxyl

concentration at the edges of each sample and in the middle. While some data deviate somewhat from the fitted curves, they fall mostly within the uncertainty limits of the measurements. These deviations often resulted from small imperfections, such as conchoidal fractures on the sample corners or small surface fractures.

Figure 4 shows chemical diffusivities for hydrogen incorporation as a function of temperature for diffusion parallel to each of the crystal axes. Only diffusion coefficients with errors lower than 30% for diffusion parallel to [001] and lower than 50% for diffusion parallel to [010] and [100] are plotted in the figure and were used to calculate activation energies. While the data for diffusion parallel to [001] and [010] for the experiments at 1.5 GPa agreed well with those from experiments at 0.2 GPa, the data on diffusion parallel to [100] for both Fo1-3 and Fo2-2 (the hollow circles in Fig. 4) are significantly faster than those from the lower-pressure experiments, and were not used in the activation energy calculations. While a possible anisotropic dependence of diffusivity on pressure is intriguing, quantification of such an effect is beyond the scope of the present work. The remaining data were fit using a least-squares regression to the Arrhenius relation:

$$\tilde{D}_i = \tilde{D}_i^{\circ} \exp(-Q_i/\mathrm{R}T), \tag{6}$$

where $\tilde{D}_i$ is the chemical diffusion coefficient parallel to i = [100], [010] or [001], $\tilde{D}_i^{\circ}$ is the pre-exponential term and Q_i is the activation energy for diffusion. Using Eq. (6), we determined activation energies and pre-exponential terms for chemical diffusion of 210 ± 33 kJ mol^{-1} and $10^{-3.3\pm1.3}$ m^2 s^{-1} for diffusion parallel to [001], 205 ± 31 kJ mol^{-1} and $10^{-4.1\pm1.2}$ m^2 s^{-1} for diffusion parallel to [010], and 225 ± 40 kJ mol^{-1} and $10^{-3.8\pm1.6}$ m^2 s^{-1} for diffusion parallel to [100].

As the calculated activation energies for chemical diffusion are, within error, the same for all directions, we performed a global fit to all data for all directions and determined an activation energy for chemical diffusion of 211 ± 18 kJ mol^{-1} and pre-exponential terms of $10^{-3.3\pm0.7}$ m^2 s^{-1} parallel to [001], $10^{-3.9\pm0.7}$ m^2 s^{-1} parallel to [010], and $10^{-4.4\pm0.7}$ m^2 s^{-1} parallel to [100]. The global fit was performed by varying the activation energy and pre-exponential

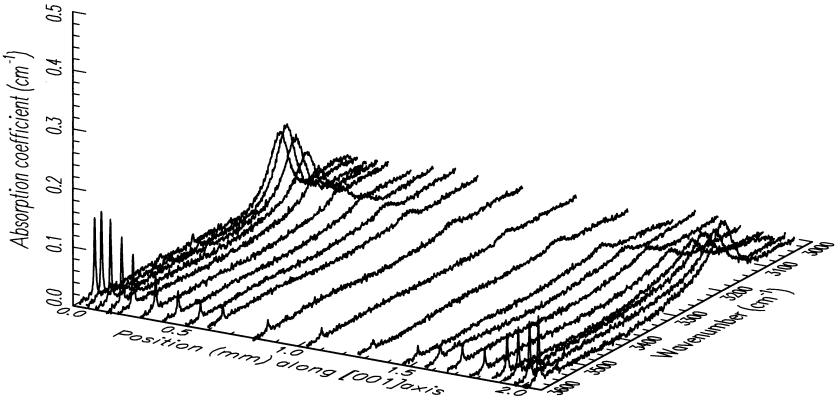

Fig. 2 Series of polarized infrared spectra with **E** // [001] as a function of position parallel to [001] in sample Fo2-9 after an experiment at 0.2 GPa, 1110 °C, for 3 h buffered with Ni–NiO

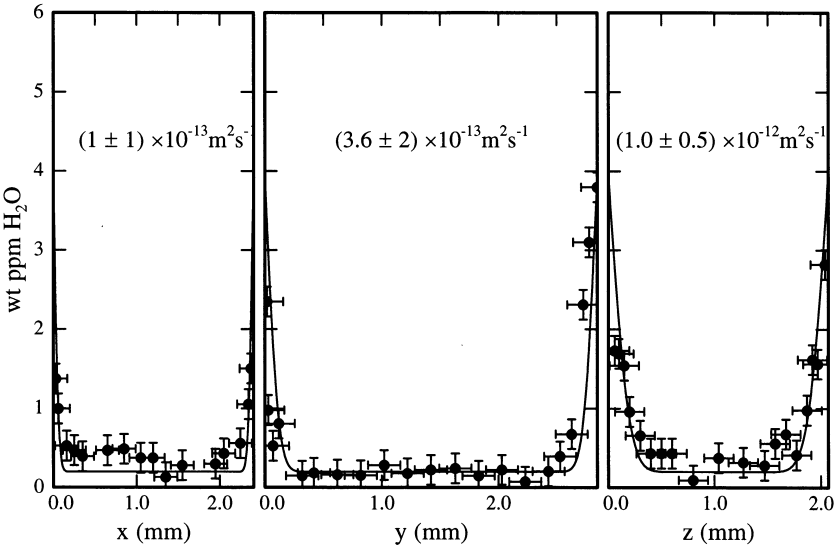

Fig. 3 Water content as a function of position parallel to each crystallographic axis (x = [100], y = [010], z = [001]) for the sample Fo2-10 after a hydrogenation experiment at 0.2 GPa, 1110 °C, 3 h, buffered with Ni–NiO. The *solid curves* represent the solution to the diffusion law presented in Eq. (3). The chemical diffusion coefficient, $\tilde{D}$, is given for each axis

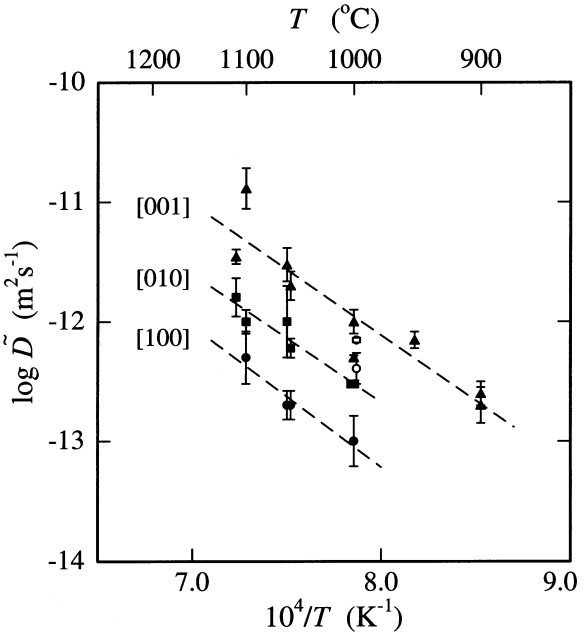

Fig. 4 Chemical diffusivity for hydrous defect incorporation in forsterite. The solid symbols are our results from the hydrogen incorporation process for axes [100], [010] and [001]. The *dashed lines* represent the best linear least-squares fit to the data for each axis

terms until the root-mean-square deviation of the fit from the data was minimized.

Discussion

Infrared band positions and water solubility

Table 3 presents infrared bands from this study and from previous work on iron-bearing olivine (Bai and Kohlstedt 1993; Libowitzky and Beran 1995). Three main differences are apparent: (1) hydroxyl infrared bands in forsterite are more strongly polarized than in olivine, (2) our forsterite spectra do not show bands between 3680 and 3620 cm^{-1}, suggesting that these bands could represent hydrogen linked to iron-related point defects, (3) a strong band is situated at 3155 cm^{-1} in sample Fo2 and at 3215 cm^{-1} in sample Fo1-3, in both cases with **E** parallel to [001]. Although Libowitsky and Beran (1995) mentioned a very weak band at 3215 cm^{-1}, such a strong band has not been observed previously in this wavenumber range. The source of this band is unlikely to be due to sample contamination, as the forsterite samples are still perfectly transparent after the experiments and contamination from the buffer powders was not detected by electron microprobe analysis.

An alternative source of this band could be hydrogen-boron defects, as there is certainly abundant boron in the Fo2 forsterite crystal. Unfortunately, there was not enough hydrated Fo2 material to perform middle-infrared analysis (MIR) using KBr pellets in the wavenumber range 760–530 cm^{-1} to check for $[B(OH)_4]^-$ and to compare with the spectra of Sykes et al. (1994). Sufficient material was also not available to perform ICP-AES analysis of the Fo1 crystal to check the boron content. In addition, the effect of boron on hydroxyl band positions and Pauling's substitution with Si is difficult to estimate because of its chemical properties with a small ionic radius and polyvalent cationic state. Thus, although hydrogen-boron-associated defects are likely in our crystals, we cannot definitively claim these as source of the hydroxyl bands in forsterite at 3215 and 3155 cm^{-1}.

In previous studies the infrared bands, based mostly on bond orientations, have been variously assigned as hydrogen–metal vacancy- or hydrogen–silicon vacancy-associated defects (e.g. Beran and Putnis 1983; Freund and Oberheuser 1986; Matveev et al. 2001; Locke et al. 2002). In the recent work of Matveev et al. (2001), hydroxyl bands between 3380 and 3285 cm^{-1} were assigned as hydrogen linked to metal vacancies whereas hydroxyl bands at higher frequencies 3640–3430 cm^{-1} and at 3295 cm^{-1} were attributed to hydrogen substitution in tetrahedral (silicon) sites. Unfortunately, direct association of hydroxyl infrared bands with specific point defects remains controversial and our results do not permit discrimination between the defect models. The fact that all bands seem to be incorporated into forsterite at similar rates is suggestive of, but certainly does not guarantee, a single diffusive species.

When FTIR spectroscopy is used to quantify water content, a calibration has to be applied to the spectra to determine the water concentration. The verity of the various calibrations is a source of ongoing debate (Paterson 1982; Bell et al. 1995; Libowitzky and Rossman 1996; Bell et al. 2003). In our analysis, we used Eq. (1) and the calibration of Bell et al. (2003). It is noteworthy, however, that as the diffusion shows no concentration dependence, the choice of infrared calibration will have no effect on the calculated diffusivities (Kohlstedt and Mackwell 1998).

Diffusion in forsterite

On the assumption that hydrogen self-diffusion is much faster than metal-vacancy diffusion (Kohlstedt and Mackwell 1998), we used Eq. (5) to determine the diffusivities for metal vacancies from the chemical diffusivities. Figure 5 presents diffusion rates as functions of temperature from this study, as well as from previous work on transport of water-derived species, metal vacancies and electron holes in olivine (Nakamura and Schmalzried 1983; Sato 1986; Mackwell and Kohlstedt 1990; Kohlstedt and Mackwell 1998). Our results are in good agreement with previous work on metal vacancy diffusion in iron-bearing olivine using (1) water as a tracer, as in this study (KM in Fig. 5; Kohlstedt and Mackwell 1998), (2) reequilibration rates from deformation and electrical conductivity experiments

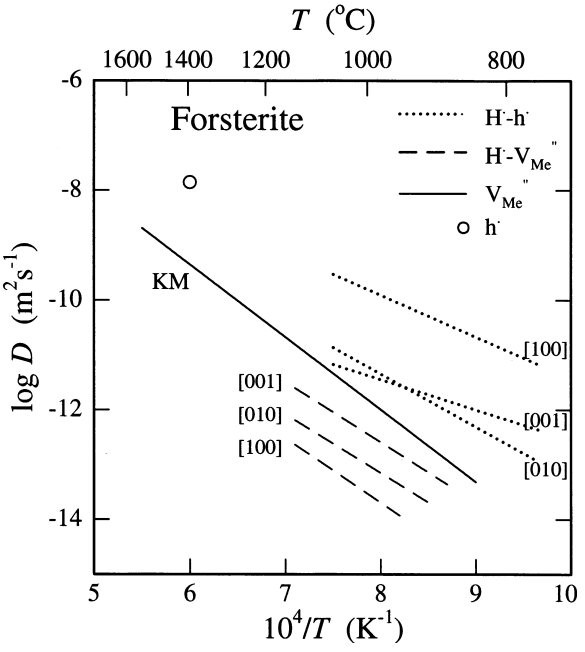

Fig. 5 Diffusivities for metal vacancy and hydrogen ions in olivine and forsterite. The *dashed lines* are our metal vacancy diffusivities assuming hydrogen incorporation process linked to metal-vacancy transport. The *dotted lines* represent the results from Kohlstedt and Mackwell (1998) for hydrogen diffusion during redox exchange in olivine. The *solid line* represents the linear fit to the compilation of data for metal vacancy diffusion in iron-bearing olivine from previous publications (Nakamura and Schmalzried 1983, 1984; Mackwell et al. 1988; Kohlstedt and Mackwell 1998). The *circle* represents the polaron diffusivity calculated by Sato (1986) from electrical conductivity measurements

(Mackwell et al. 1988; Wanamaker 1994), (3) electrical conductivity measurements of Constable and Duba (2002) and (4) Fe-Mg interdiffusion and thermal balance measurements (Nakamura and Schmalzried 1983, 1984). Compared with the previous work on diffusion of hydrogen-metal vacancy diffusion in iron-bearing olivine (Kohlstedt and Mackwell 1998), although the diffusivities are a little slower for the same orientation and temperature, the anisotropy in diffusion of hydrogen-metal vacancy defects is the same as in iron-bearing olivine, with fastest diffusion parallel to [001] (Fig. 5). Parallel to [001], the activation energy for diffusion is 210 ± 33 kJ mol^{-1} compared to 260 ± 20 kJ mol^{-1} for olivine (Kohlstedt and Mackwell 1998).

Point defects in forsterite

End-member forsterite (Mg_2SiO_4) is near-stoichiometric and an insulator. Deviations from stoichiometry are expected to result from thermal Frenkel defects on the metal sublattice (e.g. Stocker 1978; Stocker and Smyth 1978). At the relatively low homologous temperatures of our experiments defect concentrations are likely only at sub-ppm levels. However, as noted above, boron may play a significant role in the point-defect chemistry of our forsterite, as it is the majority impurity species. While we can hypothesize that it mostly exists in the $+3$ valence, is a substitutional defect in silicon sites and is charge compensated by metal vacancies, its detailed speciation is not known with certainty. Should the boron reside mostly in the silicon sites, a logical role for hydrogen would be to charge-compensate the boron, making hydrogen-boron associates a favoured defect in the structure of synthetic forsterite.

Given that the rate and anisotropy of diffusion are similar to those for iron-bearing olivine, it seems reasonable to assume that the same diffusion mechanism is involved in forsterite (Kohlstedt and Mackwell 1998). Thus, incorporation of water into the forsterite structure at ppm levels requires the cooperative incorporation of other defects, probably metal (octahedrally coordinated) or silicon (tetrahedrally coordinated) vacancies. The consequent concentration of vacancies (metal or silicon) is thus significantly higher when associated with water than under dry conditions. The concentrations of such defects, as indicated by the hydroxyl concentrations in our samples, are similar to, if a little lower than, in iron-bearing olivine. Thus, the concentration of hydrogen-vacancy-associated defects is not highly dependent on iron content.

Interestingly, the stabilization of higher concentrations of vacancies (metal or silicon) by the presence of water-derived species should act to increase the diffusivities of the appropriate cations in the forsterite structure. Thus, if the defects are mostly hydrogen-metal vacancy-associated pairs, we might anticipate a significant increase in magnesium diffusion or iron-magnesium interdiffusion in a hydrous environment. On the other hand, if the defects are mostly hydrogen-silicon vacancies, we might expect a major weakening of the mechanical behaviour of forsterite under wet conditions.

Geological implications

The diffusion rates calculated in the study are slow relative to times for xenoliths to be entrained and brought to the surface but fast in comparison to the times for ascent of mantle plumes. Thus, we expect some modification of the original mantle water content in xenoliths but incomplete reequilibration to the new (hydrous or anhydrous) environment. Consequently, water solubility in xenolithic olivine crystals is at best only a partial reflection of the last geological event in an olivine's life.

Conclusions

The hydrogenation experiments reported in this study provide further insight into the interactions of olivine with water under conditions appropriate to the interior

of the Earth. In particular, we have demonstrated the following:

1. Very rapid hydrogenation with fastest diffusion parallel to [100], as described previously by Mackwell and Kohlstedt (1990) for iron-bearing olivine, does not occur in iron-free forsterite, supporting the model of proton-polaron exchange for this process.
2. Hydrogenation results for forsterite with fastest diffusion parallel to [001] are similar to previous data for olivine (Kohlstedt and Mackwell 1998), which were interpreted as incorporation of proton-metal vacancy-associated defects. These new results are thus consistent with incorporation of water-derived species rate limited by the diffusivity of metal vacancies. It is also conceivable that the mobile defects are hydrogen-silicon vacancy associates.
3. Diffusion is only modestly slower in forsterite than in olivine under the same conditions. Thus, the transport of water-derived species in olivine is not strongly coupled to the iron concentration, in contrast to measurements of hydrogen solubility, which increase with increasing iron content (Zhao et al. 2001).
4. Iron content also does not affect anisotropy of diffusion, with results for both iron-free forsterite and iron-bearing olivine, yielding:

$$\tilde{D}_{[001]} > \tilde{D}_{[010]} > \tilde{D}_{[100]}.$$

5. From the experimental results and assuming a model of hydrogen–metal vacancy defects, where the vacancies are the slower diffusing species, metal-vacancy diffusion parallel to each crystallographic direction in forsterite can be described by:

$$D_{V_{Me[001]}} = 10^{-(3.8\pm1.3)} \exp[-(210 \pm 33)/RT]$$

$$D_{V_{Me[010]}} = 10^{-(4.6\pm1.2)} \exp[-(205 \pm 31)/RT]$$

$$D_{V_{Me[100]}} = 10^{-(4.3\pm1.6)} \exp[-(225 \pm 40)/RT]$$

6. Equilibration of forsterite or olivine crystals to a change in the hydrothermal environment can be expected to take significantly longer than predicted from hydrogen self-diffusion in olivine, as it requires transport of hydrogen-bearing defect associates, which are rate-limited by the transport of slower defects, such as metal vacancies.

Acknowledgements The authors thank Mervyn Paterson for supplying the Fo2 forsterite crystal, Hans Keppler and Burkhart Schmidt for their help with the infrared spectrometer and the TZM cold-seal vessels, Falko Langenhost for the TEM observations and Anke Markert for the ICP-AES analysis. The authors would like also to thank James Tyburczy and an anonymous reviewer for their constructive reviews. This work was supported by the European Community through the Human Potential Programme HPRN-CT-2000-00056, HydroSpec.

References

Arndt NT, Ginibre C, Chauvel C, Albarède F, Cheadle M, Herzberg C, Jenner G, Lahaye Y (1998) Were komatiites wet? Geology 26: 739–742

Bai Q, Kohlstedt DL (1992) Substantial hydrogen solubility in olivine and implications for water storage in the mantle. Nature 357: 672–674

Bai Q, Kohlstedt DL (1993) Effects of chemical environment on the solubility and incorporation mechanism for hydrogen in olivine. Phys Chem Miner 19: 460–471

Bell DR, Rossman GR (1992) Water in Earth's mantle: the role of nominally anhydrous minerals. Science 255: 1391–1397

Bell DR, Ihinger PD, Rossman GR (1995) Quantitative and analysis of trace OH in garnet and pyxoxenes. Am Mineral 80: 465–474

Bell DR, Rossman GR, Maldener J, Endisch D, Rauch F (2003) Hydroxide in olivine: a quantitative determination of the absolute amount and calibration of the IR spectrum. J Geophys Res 108: B2, doi: 10.1029/2001JB000679

Beran A, Putnis A (1983) A model of the OH position in olivine, derived from infrared-spectroscopy investigations. Phys Chem Miner 9: 57–60

Brunner GO, Wondratschek H, Laves F (1961) Ultrarotuntersuchungen über den Einbau von H in natürlichem Quarz. Z Elektrochem 65: 735–750

Carslaw HS, Jaeger JC (1959) Conduction of head in solids, 2nd ed. Clarendon, Oxford, 510 pp

Chopra PN, Paterson MS (1984) The role of water in the deformation of dunite. J Geophys Res 89: 7861–7876

Constable S, Duba A (2002) Diffusion and mobility of electrically conducting defects in olivine. Phys Chem Miner 29: 446–454

Freund F, Oberheuser G (1986) Water dissolved in olivine. J Geophys Res 91: 745–761

Gaetani GA, Grove TL (1998) The influence of water on melting of mantle peridotite Contrib Mineral Petrol 131: 323–346

Ingrin J, Skogby H (2000) Hydrogen in nominally anhydrous upper-mantle minerals: concentration levels and implications. Eur J Mineral 12: 543–570

Karato SI, Paterson MS, Fitz Gerald JD (1986) Rheology of synthetic olivine aggregates: influence of grain size and water. J Geophys Res 91: 8151–8176

Kohlstedt DL, Mackwell SJ (1998) Diffusion of hydrogen and intrinsic point defects in olivine. Z Phys Chem 207: 147–162

Kohlstedt DL, Mackwell SJ (1999) Solubility and diffusion of "water" in silicate minerals. In: Catlow R (ed) Microscopic properties and processes in minerals. Kluwer Academic, The Netherlands, pp 539–559

Kohlstedt DL, Keppler H, Rubie DC (1996) Solubility of water in the α, β and γ phases of $(Mg,Fe)_2SiO_4$. Contrib Mineral Petrol 123: 345–357

Libowitzky E, Beran A (1995) OH defects in forsterite. Phys Chem Miner 22: 387–392

Libowitzky E, Rossman GR (1996) Principles of quantitative absorbance measurements in anisotropc crystals. Phys Chem Miner 23: 319–327

Locke DR, Holloway JR, Hervig R (2002) Oxidation-independent solution mechanism for hydrogen in olivine: examples from simple and peridotite systems. EOS Trans AGU 83: F1380

Mackwell SJ, Kohlstedt DL (1990) Diffusion of hydrogen in olivine: implications for water in the mantle. J Geophys Res 95: 5079–5088

Mackwell SJ, Kohlstedt DL, Paterson MS (1985) The role of water in the deformation of olivine single crystals. J Geophys Res 90: 11319–11333

Mackwell SJ, Dimos D, Kohlstedt DL (1988) Trancient creep of olivine: point-defect relaxation times. Philos Mag (A) 57: 779–789

Matveev S, O'Neill HStC, Ballaus C, Taylor WR, Green DH (2001) Effect of silica activity on OH^- IR spectra of olivine:

implications for Low-$a$$SiO_2$ mantle metasomatism. J Petrol 42: 721–729

Miller GH, Rossman GR, Harlow GE (1987) The natural occurrence of hydroxide in olivine. Phys Chem Miner 14: 461–472

Muentener O, Kelemen PB, Grove TL (2001) The role of H_2O during crystallization of primitive arc magmas under uppermost mantle conditions and genesis of igneous pyroxenites: an experimental study. Contrib Mineral Petrol 141: 643–658

Nakamura A, Schmalzried H (1983) On the nonstoichiometry and point defects of olivine. Phys Chem Miner 10: 27–37

Nakamura A, Schmalzried H (1984) On the Fe^{2+}–Mg^{2+} interdiffusion in olivine (II). Ber Bunsen Phys Chem 88: 140–145

O'Neill HStC (1987) Free energies of formation of NiO, CoO, Ni_2SiO_4, and Co_2SiO_4. Am Mineral 72: 280–291

O'Neill HStC, Wall VJ (1987) The olivine-orthopyroxene-spinel oxygen geobarometer, the nickel precipitation curve, and the oxygen fugacity of Earth's upper mantle. J Petrol 28: 1169–1191

Paterson MS (1982) The determination of hydroxyl by infrared absorption in quartz, silicate glasses and similar materials. Bull Minéral 105: 20–29

Philibert J (1991) Atom movement, diffusion and mass transport in solids. Les éditions de physiques, les Ullis, France, 577 pp

Raterron P, Chopra P, Doukhan JC (2000) SiO_2 precipitation in olivine: ATEM investigation of two dunites annealed at 300 MPa in hydrous conditions. Earth Planet Sci Lett 180: 415–423

Sato H (1986) High temperature a.c. electrical properties of olivine single crystal with varying oxygen partial pressure: implications for the point-defect chemistry. Earth Planet Inter 41: 269–282

Stocker RL (1978) Point-defect formation parameters in olivine. Phys Earth Planet Inter 17: 108–117

Stocker RL, Smyth DM (1978) Effect of enstatite activity and oxygen partial pressure on the point-defect chemistry of olivine. Phys Earth Planet Ints 16: 145–156

Sykes D, Rossman GR, Veblen DR, Grew ES (1994) Enhanced H and F incorporation in borian olivine. Am Mineral 79: 904–908

Tsai T-L, Dieckmann R (1997) Point defect and transport of matter and charge in olivines $(Fe_xMg_{1-x})_2SiO_4$. Mat Sci Forum 239–241: 399–402

Tsai T-L, Dieckmann R (2002) Variation of the oxygen content and point defects in olivines $(Fe_xMg_{1-x})_2SiO_4$, $0.2 < x < 1.0$. Phys Chem Miner 29: 680–694

Wanamaker BJ (1994) Point-defect diffusivities in San Carlos olivine derived from reequilibration of electrical conductivity following changes in oxygen fugacity. Geophys Res Lett 21: 21–24

Zhao Y-H, Ginsberg S, Kohlstedt D (2001) Experimental investigation on water solubility in olivine single crystal with different Fe content. Acta Petrolog Sin 17: 123–128